



## Practice article

# Hierarchical control strategy for a three-phase 4-wire microgrid under unbalanced and nonlinear load conditions



Amirreza Naderipour<sup>a</sup>, Zulkurnain Abdul-Malek<sup>a,\*</sup>, Vigna K. Ramachandramurthy<sup>b</sup>, Akhtar Kalam<sup>c</sup>, Mohammad Reza Miveh<sup>d,\*</sup>

<sup>a</sup> Institute of High Voltage & High Current, School of Electrical Engineering, Faculty of Engineering, Universiti Teknologi Malaysia, 81310 Johor Bahru, Malaysia

<sup>b</sup> Institute of Power Engineering, Department of Electrical Power Engineering, Universiti Tenaga Nasional, Jalan Ikram-Uniten, Kajang 43000, Malaysia

<sup>c</sup> College of Engineering and Science, Victoria University, Melbourne 3047, Australia

<sup>d</sup> Department of Electrical Engineering, Tafresh University, Tafresh 39518-79611, Iran

## H I G H L I G H T S

- This paper proposes an improved hierarchical control strategy for a three-phase 4-wire islanded microgrid under unbalanced and nonlinear load conditions.
- The superiority of the proposed control strategy over the conventional SCC-based control scheme was confirmed by the 2 line cycles decrease in the transient response.
- The compensation of both negative and zero sequence harmonics, simple control structure and insensitivity to frequency variations have given this control scheme an edge over the conventional control strategies. The voltage THD of the grid-forming power converters were reduced from above 5.1% to lower than 2.7% with the suggested controller under nonlinear load situations.
- Zero reactive power-sharing error has given this control strategy an edge over the conventional droop control scheme in three-phase 4-wire islanded microgrids.

## A R T I C L E I N F O

### Article history:

Received 28 October 2017

Received in revised form 12 January 2019

Accepted 24 April 2019

Available online 4 May 2019

### Keywords:

Hierarchical control

Nonlinear load

Microgrid

Frequency stability

Voltage control

Islanded mode

## A B S T R A C T

This paper proposes an improved hierarchical control strategy consists of a primary and a secondary layer for a three-phase 4-wire microgrid under unbalanced and nonlinear load conditions. The primary layer is comprised of a multi-loop control strategy to provide balanced output voltages, a harmonic compensator to reduce the total harmonic distortion (THD), and a droop-based scheme to achieve an accurate power sharing. At the secondary control layer, a reactive power compensator and a frequency restoration loop are designed to improve the accuracy of reactive power sharing and to restore the frequency deviation, respectively. Simulation studies and practical performance are carried out using the DigSILENT Power Factory software and laboratory testing, to verify the effectiveness of the control strategy in both islanded and grid-connected mode. Zero reactive power sharing error and zero frequency steady-state error have given this control strategy an edge over the conventional control scheme. Furthermore, the proposed scheme presented outstanding voltage control performance, such as fast transient response and low voltage THD. The superiority of the proposed control strategy over the conventional filter-based control scheme is confirmed by the 2 line cycles decrease in the transient response. Additionally, the voltage THDs in islanded mode are reduced from above 5.1% to lower than 2.7% with the proposed control strategy under nonlinear load conditions. The current THD is also reduced from above 21% to lower than 2.4% in the connection point of the microgrid with the offered control scheme in the grid-connected mode.

© 2019 ISA. Published by Elsevier Ltd. All rights reserved.

## 1. Introduction

In spite of numerous benefits provided by large power generation plants, economical, technical and environmental advantages have led to the gradual development of small-scale power sources

\* Corresponding authors.

E-mail addresses: [zulkurnain@utm.my](mailto:zulkurnain@utm.my) (Z. Abdul-Malek), [miveh@tafreshu.ac.ir](mailto:miveh@tafreshu.ac.ir) (M.R. Miveh).

into smart grids. This new form of power generation is termed as Distributed Generation (DG). However, the increasing interest in integrating DGs and loads in the same grid, presents major challenges from the viewpoint of reliable operation and control [1]. Bidirectional power flow, stability, and power quality issues are the most relevant challenges stemming from the massive application of DGs into the distribution network [2]. Thus, the emergence of the microgrid concept is a feasible solution towards integrating DGs and loads in the same grid. Normally, the microgrid system operates in grid-connected mode. On the other hand, if any event such as general faults or long-time voltage dips happens within the main grid, the microgrid can operate in islanded mode. Voltage and frequency stability, power sharing management, and power quality control are the main challenges in microgrids. Hence, they require a proper control system for both islanded and grid-connected operations.

Microgrids require suitable control and management systems in both islanded and grid-connected modes to meet all the control objectives in a clear and systematic way. A possible solution to achieve various control objectives in microgrids is to introduce the hierarchical control structure [3]. Three main control layers can be distinguished in this control strategy, including primary, secondary and tertiary controllers. The primary control is in charge of the current and voltage regulation, low-level protection, voltage and frequency stability as well as power-sharing control. Moreover, the secondary layer is responsible for achieving global performance objectives, such as power management, black start management, grid resynchronization, voltage and frequency restoration, and reactive power compensation [2,4–6]. The secondary layer is the highest hierarchical control layer in island mode. The tertiary control level also controls the flow of power from the microgrid to the main grid [6]. This is accomplished by adjustment of the frequencies and amplitudes of the Distributed Energy Resource (DER) voltages [6,7]. It also ensures economically optimal operation of the microgrid [5–8].

Commonly, DG units used in microgrids must be able to supply a mixture of unbalanced and nonlinear loads via a three-phase 4-wire distribution network [9,10]. Such conditions can lead to various stability, reliability, and power quality difficulties for islanded microgrids. The control system of an islanded microgrid has several functions, including voltage and frequency management, load sharing between distributed systems, and power quality control. These tasks become more complicated under unbalanced and nonlinear load circumstances. Imbalanced phases, harmonic contents in the waveform, variations in magnitude and frequency, and inaccurate active and reactive power sharing are the key challenges associated with islanded microgrids under such conditions. According to the IEEE Standard 1159, the Phase Voltage Unbalanced Rate (PVUR) should be maintained below 2% for unbalanced loads [11,12]. Moreover, according to the IEEE Standard 519–2014, the voltage Total Harmonic Distortion (THD) should be maintained below 5% for nonlinear loads [13]. To date, various methods have been developed to control islanded microgrids under unbalanced and nonlinear load conditions. A simple method for unbalanced and nonlinear load compensation is without using Active Power Filters (APFs) [14], nonetheless, it is not the best solution due to complex control system and economic issues. Therefore, the use of grid-forming power converters can be one of the best solution for compensating unbalanced and nonlinear loads.

Numerous control approaches, containing the hysteresis control [15], repetitive feedback control [16], the Finite Control Set Model Predictive Control (FCS-MPC) [17], Sliding Mode Control (SMC) [18–20], Proportional Resonant (PR) controllers [21], Proportional Integral (PI) controller based on Symmetrical Components Calculators (SCCs) [22–24], have been proposed in the

literature to improve the power quality of microgrids and distribution networks under abnormal conditions. However, these control techniques for four-leg inverters often suffer from slow transient response, coupling between phases, complex control algorithm, and unsatisfactory steady-state voltage tracking error. Furthermore, for three-phase 4-wire microgrids, harmonics controllers are not as well-established as three-phase 3-wire applications due to the presence of both zero and negative sequence harmonics. Complex control algorithms and sensitivity to frequency variations in the islanding mode are other disadvantages discovered by previous studies in reducing the voltage THD in three-phase 4-wire islanded microgrids. Hierarchical control of three-phase 3-wire islanded microgrids under unbalanced and nonlinear load conditions is a well-developed research topic. Nevertheless, far too little attention has been paid to the hierarchical control of three-phase 4-wire islanded microgrids under unbalanced and nonlinear load conditions. Therefore, it is important to propose improved primary and secondary control schemes for three-phase 4-wire islanded microgrids to achieve zero active and reactive power-sharing error, balanced output voltage with low THD and zero voltage/frequency steady-state error under abnormal load conditions.

This research proposes an enhanced hierarchical control approach for a three-phase 4-wire microgrid using four-leg power converters under unbalanced and nonlinear load conditions. The primary layer comprised of a per-phase multi-loop control strategy, a multi-resonant harmonic, and a droop-based power sharing control scheme. At the secondary control layer, a reactive power compensator and a frequency restoration loop are designed using low bandwidth communication links to improve the accuracy of the reactive power sharing and restore the frequency deviation caused by the primary layer, respectively. The rest of this study is organized as follows. Section 2 presents the primary layer, including the current–voltage control strategy, the multi-resonant harmonic compensator and the droop-based control scheme. The secondary control scheme is presented in Section 3. Simulation results are given in Section 4. Finally, the conclusion is made in the last section.

## 2. Primary control

The primary layer of proposed controller for four-leg power converters consists of a multi-loop control strategy to provide balanced output voltages, a harmonic controller to minimize the THD, and a droop-based control scheme to attain an accurate power sharing. The primary layers of the suggested controller are explained in the following subsections.

### 2.1. Multi-loop control strategy

The structure of the suggested per-phase multi-loop control scheme for phase ‘a’ is presented in Fig. 1. As can be observed, an orthogonal signal generation technique is used to transfer the output voltage in each phase ( $V_{oa}$ ,  $V_{ob}$ ,  $V_{oc}$ ) into the  $\alpha\beta$  frame. Next, using the Park transformation the load voltage quantities in the  $\alpha\beta$  frame are transformed into the synchronous reference frame. A second-order generalized integrator frequency-locked loop (SOGI-FLL) is utilized to extract the required information for the Park transformation [25]. PI controllers are used to compensate the load voltage quantities ( $V_{a-q}$ ,  $V_{a-d}$ ) by comparing the reference voltage values ( $V_q^*$ ,  $V_d^*$ ) in the dq frame. To achieve this objective,  $V_d^*$  is set at the peak value of the reference phase voltage and  $V_q^*$  is set at 0 V. The reference signals for the current controllers is provided from the outputs of the external voltage loop. The generated references for the current controller via the voltage regulator are then converted from the dq frame into

the  $\alpha\beta$  frame ( $i_{ca,\alpha}^*$ ). As seen, the inner current control loop is implemented in the stationary reference frame. Consequently, only the real reference current ( $i_{ca,\alpha}^*$ ) is fed to the current controller. Moreover, the capacitor current ( $i_{ca}$ ) is sampled, and then compared with the reference currents made by the outer voltage controller. In the  $\alpha\beta$  frame, the reference signals are sinusoidal; therefore, a proportional controller can be used to guarantee the outstanding reference tracking and to attain a zero steady-state error.

Furthermore, in order to improve the system robustness a voltage feedforward path ( $v_a^*$ ) is added to the controller. The decoupling voltage feedback path is also used in the controller to reduce the effect of power stage coupling. Finally, the output of the current controller ( $V_{af}, V_{bf}, V_{cf}$ ) is converted into the abc frame to provide three-phase voltage reference for the pulse width modulator (PWM). As  $V_{dc}$  is not constant, a feedforward loop is included to consider the DC-link voltage value for the generation of the gate signals. This way, deviations of  $V_{dc}$  inside the allowed limits can be compensated. Furthermore, the carrier-based PWM method is used in this paper to generate the inverter output voltage owing to its proper performance and ease of implementation. In the offered control scheme, the PI controller adjusts the output voltages in the dq frame. Moreover, the simple proportional controller adjusts the currents in the  $\alpha\beta$  frame. Same strategy is applied for phase ‘b’ and ‘c’.

2.1.1. Current controller design

The block diagram of the suggested control approach with the current controller and proportional controller is depicted in Fig. 2. The closed-loop transfer function of the current controller for phase ‘a’ is:

$$G(s) = \frac{i_{ca}}{i_{ca}^*} = \frac{C_a Z K s}{L_a C_a Z s^2 + (C_a Z (r_a + K) + L_a) s + (r_a + Z)} \quad (1)$$

By considering that, the bandwidth of the inner current controller is highly important in choosing the gain of the proportional controller, the Bode diagrams of the related transfer function is presented in Fig. 3. In this respect, for the nominal load circumstance, the lowest control bandwidth can be obtained and the proportional gain must be regular under the nominal loading conditions to guarantee the predictable bandwidth under all loading circumstances. The proportional gain can be designed by  $|G(j\omega_{bi})|^2 = 1/2$ , and considering  $\omega_{bi}$  is the necessary bandwidth for the inner control loop. Therefore, the proportional gain is [26]:

$$K = \frac{L_a + r_a C_a Z + \sqrt{2r_a C_a Z (r_a C_a Z + L_a) + L_a^2 (2 + C_a^2 Z^2 \omega_{bi}^2)}}{C_a Z} \quad (2)$$

The essential bandwidth is selected 1/5 of the switching frequency for crossover frequency constraint. Considering  $f_s = 5$  kHz, the bandwidth is  $\omega_{bi} = 2\pi(0.25 \times 5)$  kHz  $\cong 8$  krad/s, and the proportional gain is adjusted on 1 by Eq. (2).

2.1.2. Voltage controller design

Since tuning of the voltage controller in the rotating frame is difficult, the stationary reference frame equivalent model of the PI compensator in the rotating reference frame is derived. The parameters of the voltage controller using a step-by-step systematic design procedure are determined. The equivalent model of the PI controller can be considered as a two-input-two-output system. Thus, it can be explained in the time domain as:

$$\begin{bmatrix} i_{c,\alpha}^*(t) \\ i_{c,\beta}^*(t) \end{bmatrix} = \begin{bmatrix} \cos(\omega_f t) & -\sin(\omega_f t) \\ \sin(\omega_f t) & \cos(\omega_f t) \end{bmatrix} \left\{ \begin{bmatrix} G_{PI}(t) & 0 \\ 0 & G_{PI}(t) \end{bmatrix} * \begin{bmatrix} \cos(\omega_f t) & \sin(\omega_f t) \\ -\sin(\omega_f t) & \cos(\omega_f t) \end{bmatrix} \begin{bmatrix} E_\alpha(t) \\ E_\beta(t) \end{bmatrix} \right\} \quad (3)$$

where \* is the convolution operator.

The Laplace transformation is used for both sides of (3); therefore, it can be rewritten as:

$$\begin{bmatrix} i_{c,\alpha}^*(s) \\ i_{c,\beta}^*(s) \end{bmatrix} = \frac{1}{2} \begin{bmatrix} G_{PI}(s + j\omega_f) + G_{PI}(s - j\omega_f) & -jG_{PI}(s + j\omega_f) + jG_{PI}(s - j\omega_f) \\ +jG_{PI}(s + j\omega_f) - jG_{PI}(s - j\omega_f) & G_{PI}(s + j\omega_f) + G_{PI}(s - j\omega_f) \end{bmatrix} \begin{bmatrix} E_\alpha(s) \\ E_\beta(s) \end{bmatrix} \quad (4)$$

In this regard,  $G_{PI}$  can be replaced by  $K_p + \frac{K_i}{s}$ , therefore:

$$\begin{bmatrix} i_{c,\alpha}^*(s) \\ i_{c,\beta}^*(s) \end{bmatrix} = \begin{bmatrix} K_p + \frac{K_i s}{s^2 + \omega_f^2} & -\frac{K_i \omega_f}{s^2 + \omega_f^2} \\ \frac{K_i \omega_f}{s^2 + \omega_f^2} & K_p + \frac{K_i s}{s^2 + \omega_f^2} \end{bmatrix} \begin{bmatrix} E_\alpha(s) \\ E_\beta(s) \end{bmatrix} \quad (5)$$

Lastly, the transfer function of the real system can be obtained by replacing  $E_\beta(s) = ((\omega_f - s)/(\omega_f + s))E_\alpha(s)$  as:

$$i_{c,\alpha}^*(s) = \frac{a_3 s^3 + a_2 s^2 + a_1 s + a_0}{s^3 + \omega_f s^2 + \omega_f^2 s + \omega_f^3} E_\alpha(s) = H(s)E_\alpha(s) \quad (6)$$

where  $a_3 = K_p$ ,  $a_2 = K_p \omega_f + K_i$ ,  $a_1 = K_p \omega_f^2 + 2\omega_f K_i$ ,  $a_0 = K_p \omega_f^3 - K_i \omega_f^2$  and  $H(s)$  indicates the stationary frame representation of the PI controller in the dq frame. Fig. 4 shows the Bode plot of transfer function  $H(s)$  for  $K_p = 0.1$ ,  $K_i = 10$  and  $\omega_f = 2\pi 60$  rad/s. As seen, the phase and amplitude characteristics of the PI controller in the dq frame are equivalent to the PR controller in the stationary reference frame at the fundamental frequency.

Fig. 5 shows the block diagram of the offered controller for phase ‘a’. In the figure,  $v^* = v_a^* = v_d^* \cos(\omega_f t) - v_q^* \sin(\omega_f t)$  is the voltage feedforward path to improve the system robustness. Note that the inner control loop is replaced by  $G(s)$  as shown in Fig. 6.

Fig. 7 shows the Bode plots of the open-loop transfer function of the controller for  $K = 1$ ,  $K_p = 0.1$  and  $K_i = 0$ . From the figure it can be seen that the stability of the closed-loop system, and the phase margin under light-load situation are reduced. Therefore, to guarantee the suitable performance of the controller in all load conditions, the PI regulator is designed under light-load condition. As under light-load condition, the load impedance ( $Z$ ) tends to infinity ( $\infty$ ), the transfer function of the current controller can be estimated as:

$$\frac{i_{ca}}{i_{ca}^*} \cong \frac{K}{L_a s + r_a + k} \quad (7)$$

Moreover, the open-loop and closed-loop transfer functions of the control system are:

$$\begin{aligned} \frac{v_{oa}}{v_a^* - v_{oa}} &= \frac{K(a_3 s^3 + a_2 s^2 + a_1 s + a_0)}{L_a C_a s^5 + b s^4 + b \omega_f s^3 + b \omega_f^2 s^2 + (r_a + K) C_a \omega_f^3 s} \quad (8) \\ \frac{v_{oa}}{v_a^*} &= \frac{K(a_3 s^3 + a_2 s^2 + a_1 s + a_0)}{L_a C_a s^5 + b s^4 + (b \omega_f + K a_3) s^3 + (b \omega_f^2 + K a_2) s^2 + ((r_a + K) C_a \omega_f^3 + K a_1) s + K a_0} \quad (9) \end{aligned}$$

The proportional gain is selected so that the needed bandwidth ( $\omega_{bv}$ ) can be attained for the closed-loop transfer functions. The integral gain is also selected to guarantee the minimum steady-state error for the outer loop. The choice of the proportional gain is accomplished based on this assumption that the dynamic of the voltage loop is unaffected by the integral

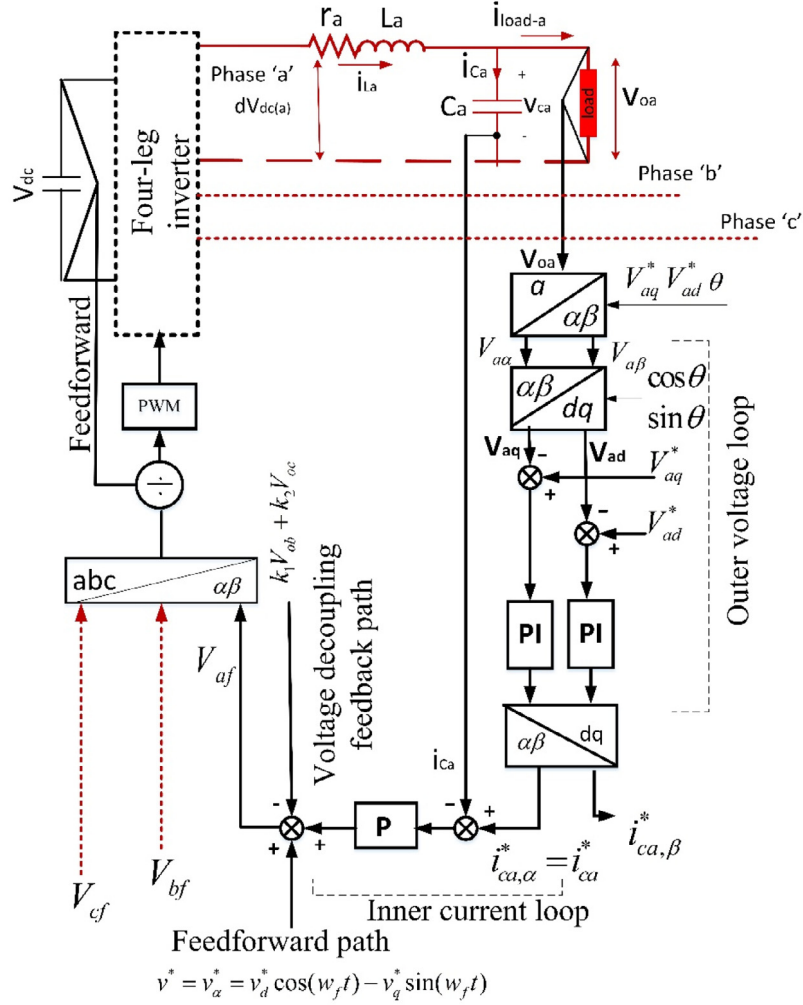


Fig. 1. Proposed per-phase multi-loop control strategy for phase 'a'.

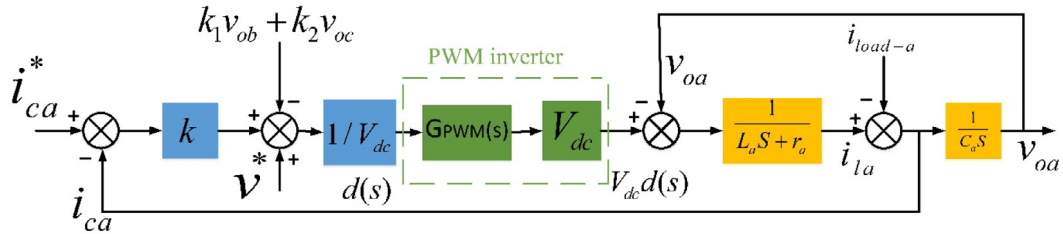


Fig. 2. Block diagram of inner current control loop.

gain. The proportional gain is in charge for the transient performance, while the performance of the controller in the steady-state is determined by the integral parameter at the fundamental frequency. Therefore,  $K_i = 0$ , during tuning the proportional parameter and the transfer function of the closed-loop system under light-load condition is:

$$\frac{v_{oa}}{v_a^*} = \frac{K_p K}{K_p K - L_a C_a \omega^2 + j(r_a + K) C_a \omega} \quad (10)$$

By considering that the bandwidth is  $\omega_{bv}$ ; so,  $K_p$  can be found as:

$$K_p = \frac{C_a \omega_{bv} [\sqrt{2L_a^2 \omega_{bv}^2 + K^2} - L_a \omega_{bv}]}{K} \quad (11)$$

In this study, the system bandwidth must be selected between 10 times of the fundamental frequency and one-tenth of the switching frequency to attain both the disturbance rejection and proper transient response. So, it is selected as 550 Hz, which is a value between 500 Hz and 600 Hz. The system bandwidth and the proportional gain are  $\omega_{bv} = 2\pi \times 550 \text{ Hz} \approx 3 \text{ krad/s}$  and 0.15, respectively. The stability analysis is applied to attain an appropriate gain for the integral regulator. The use of the Routh–Hurwitz criterion can fulfil the integrator purposes in the voltage controller. The system characteristic polynomial is:

$$L_a C_a s^5 + b s^4 + (b \omega_f + K a_3) s^3 + (b \omega_f^2 + K a_2) s^2 + ((r_a + K) C_a \omega_f^3 + K a_1) s + K a_0 = 0 \quad (12)$$

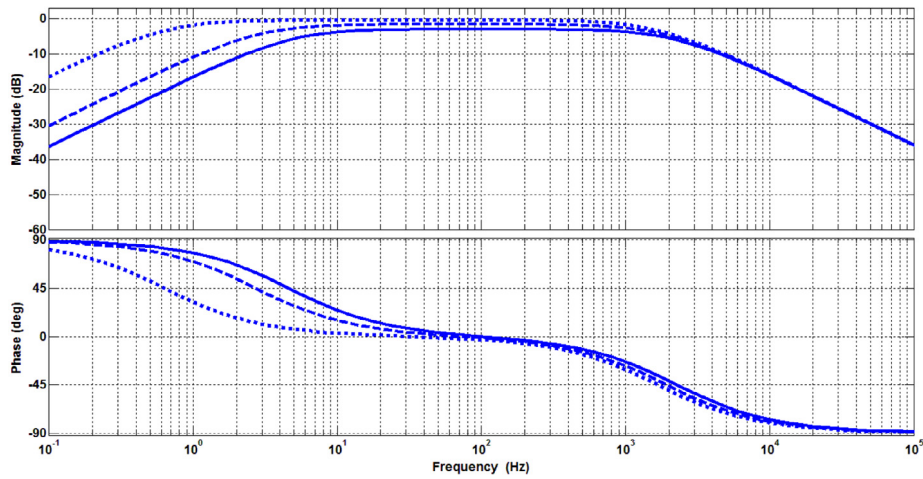


Fig. 3. Bode plots of  $G(s)$  for  $K = 1$ , under (solid line) nominal load, (dashed line) one-fifth of nominal load and (dotted line) one-tenth of nominal load.

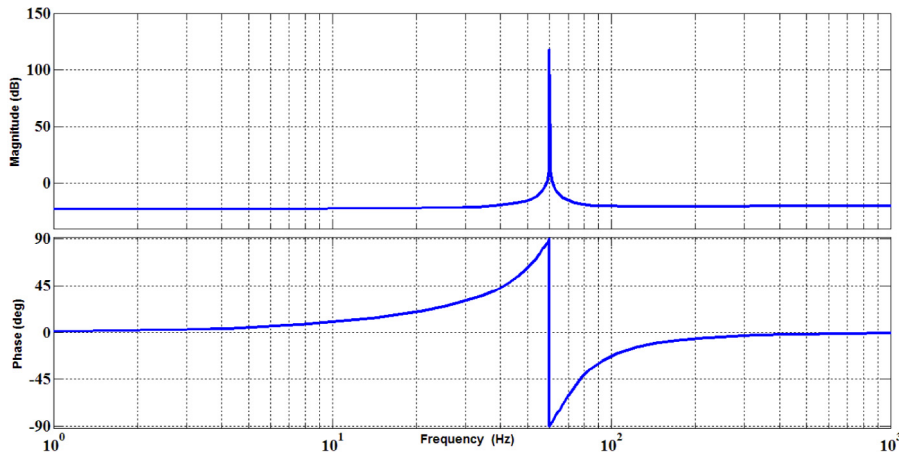


Fig. 4. Bode plot of transfer function  $H(s)$  for  $K_p = 0.1$  and  $K_i = 10$ .

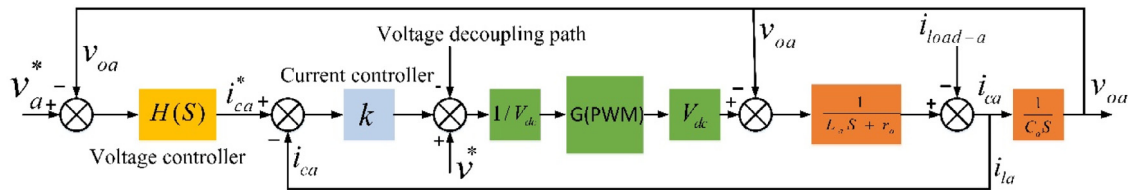


Fig. 5. Block diagram of the multi-loop control strategy for phase 'a'.

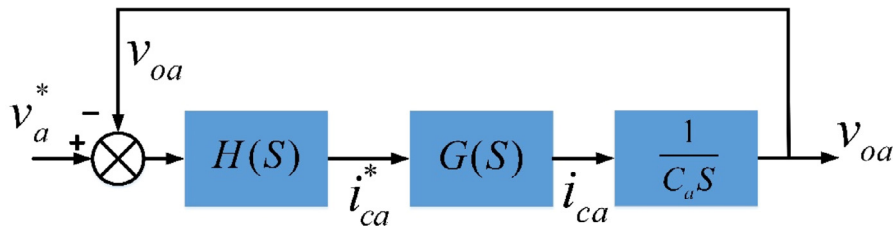


Fig. 6. The simplified representation of the control strategy for phase 'a'.

The system stability can be described as:

$$K > 0, \quad K_p > 0, \quad K_i < K_p \times \omega_f \quad (13)$$

Based on the mentioned methodology for selecting the proportional gain;  $K_p \times \omega_f$  is equal to 55. The open-loop Bode plots of  $H(s)G(s)/C_a s$  for different values of  $K_i$  are represented in

Fig. 8. From figure,  $K_i$  has no effect on the phase margin. On the other hand, an infinitive magnitude at the fundamental frequency provides a small steady-state error. However, based on the  $\alpha\beta$  frame equivalent of the PI controller in the dq frame, a high gain at the fundamental frequency can have negative effects on other frequencies. Therefore, the gain of  $K_i$  have to be selected based

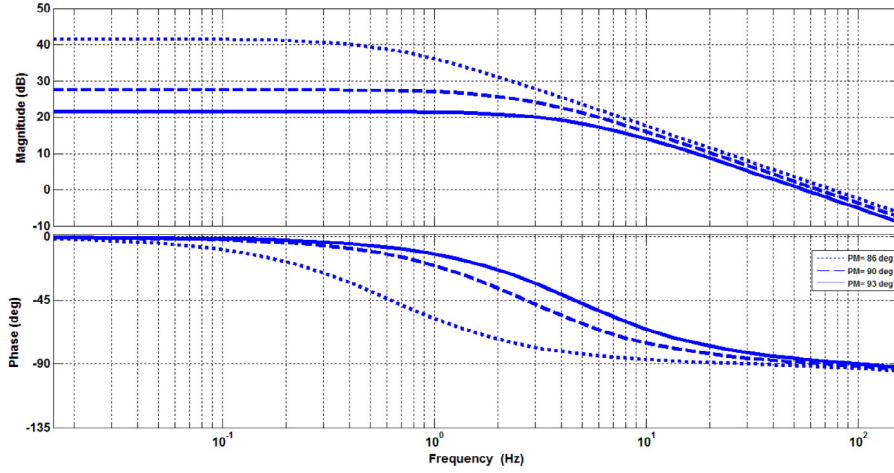


**Fig. 7.** Bode plots of  $H(s)G(s)/C_d s$ , for  $K = 1$ ,  $K_p = 0.1$ , and  $K_i = 0$ , under (solid line) nominal load, (dashed line) one-fifth of nominal load and (dotted line) one-tenth of nominal load.

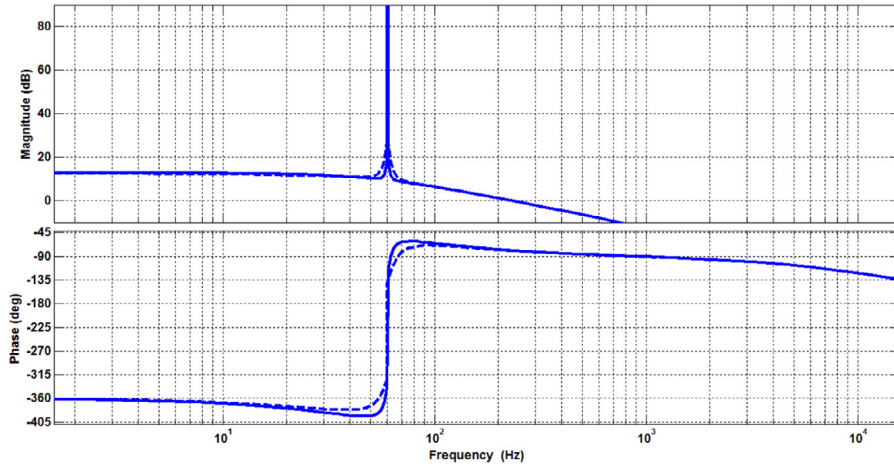


**Fig. 8.** Open-loop Bode plots of  $H(s)G(s)/C_d s$ , for  $K = 1$ ,  $K_p = 0.15$ , and  $K_i = 10$  (solid line), for  $K = 1$ ,  $K_p = 0.15$ , and  $K_i = 20$  (dashed line).

on a trade-off between reducing the steady-state error and not affecting other frequencies: thus,  $K_i$  is chosen to be 42.

### 2.2. Harmonic compensation control strategy

The transfer function of the harmonic impedance in each subsystem of the four-leg VSI can be obtained as:

$$Z_o(s) = \frac{v}{i_o} = \frac{Ls_4 + ds_3 + d\omega_f s_2 + d\omega_f^2 s + r\omega^3}{LCs_5 + bs_4 + (b\omega_f + Ka_3)s^3 + (b\omega_f^2 + Ka_2)s^2 + ((r + K)C\omega_f^3 + Ka_1)s + Ka_0} \quad (14)$$

where  $d = L\omega_f + r$

Fig. 9 shows the designed harmonic compensator added in phase ‘a’ to achieve low THD for output voltage under nonlinear load circumstances. The transfer function of the compensator can be written as:

$$HC(s) = \sum_{n=3,5,\dots,h} \frac{k_n s}{s^2 + (n\omega_f)^2} \quad (15)$$

where  $k_n$  is the gain of integrator for  $n$ th harmonic component and  $h$  is the highest harmonic order.

The proposed scheme reduces the output impedance of the power converter over the frequency range of the main harmonic

current components. The harmonic integrator must be handled both zero and negative sequence harmonics. Consequently, a harmonic compensator with six modules tuned at the 3rd, 5th, 7th, 9th, 11th and 13th harmonic frequencies is used in each phase of the inverter. The harmonic compensator gains are selected based on the stability of the whole closed-loop system. It is worth mentioning that the added resonant compensators have a very negligible effect on the dynamic performance of the inverter, since they only respond to the frequencies around their resonant frequencies.

### 2.3. Droop-based control scheme

The improved droop control approach in the primary layer is also depicted in Fig. 10. As can be seen, the three-phase four-leg terminal voltages ( $V_{out}$ ) and currents ( $I_{out}$ ) are first measured to calculate the instantaneous real and reactive powers. Then, the active and reactive powers are decoupled to provide completely decoupled control capability for the active and reactive power. The frequency of output voltage is determined using the active power/frequency ( $P - \omega$ ) loop and its dedicated droop slope ( $m_i$ ). In the same way, the reactive power regulates the magnitude of the output voltage through the reactive power/voltage ( $Q - E$ ) loop and its dedicated droop slope ( $n_i$ ). The gains of the droop controller are calculated using the method presented in [27]. A phase feedforward control loop with a proportional gain ( $k_{ff}$ ) is

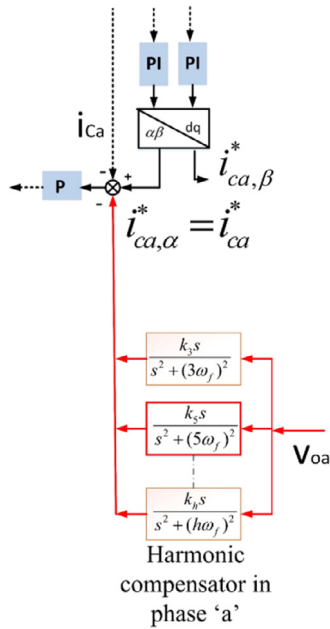


Fig. 9. Proposed harmonic compensator for phase 'a'.

also used to improve the stability of the system. The parameters of the droop controllers are given in Appendix. An additional loop is also added to  $Q - E$  loop to improve the capability of voltage regulation to accurately share the load among four-leg power converters.

Moreover, the load voltage drop  $E^* - v_o$  can be used as a feedback loop to keep the load voltage within the required limit. It is added to the  $Q - E$  loop via a proportional gain ( $k_e$ ). Since the input to the integrator in the reactive  $Q - E$  loop must be zero in the steady state, therefore [27]:

$$-n_i Q_i + k_e (E^* - v_o) = 0 \Rightarrow n_i Q_i = k_e (E^* - v_o) \quad (16)$$

The term  $k_e (E^* - v_o)$  is same for all four-leg power converters if the gain  $k_e$  is selected the same for all controllers. Hence, the term  $n_i Q_i$  is constant for all inverters operating in parallel, which guarantees precise reactive power sharing, even if the output impedance is not the same between the inverters.

### 3. Secondary controller

After a change in the load or generation, the frequency and voltage of the islanded microgrid must be changed using the primary layer to match the demand with the generation. In some circumstances, the frequency of the islanded microgrid is still below the rated value, even after the operation of the droop-based control strategy [28]. In fact, the frequency of the microgrid is sharply reduced or increased after the inclusion or disconnection of the loads. This sudden reduction or incensement is because of the action of the active power/frequency controller in DG units. In this condition, the secondary layer can regulate the difference between the rated value and the measured ones towards zero. Additionally, when the droop-based control strategy is used for the islanded microgrid, the reactive power face problem to accurately shared among DGs, since the voltage in not common in all terminals of the microgrid in contrast to the frequency.

The structure of the distributed secondary controller is depicted in Fig. 11. As seen, the secondary controller is placed

beside each primary local controller and before the communication network. It consists of a frequency restoration controller and a reactive power compensator. In this regard, frequency and reactive power are sensed through the communication network in the secondary layer, and then their average values are calculated. Subsequently, the proper control signals are generated using these control loops to compensate for the primary layer. The outputs of secondary controllers are then used in the primary controller to eliminate the steady-state errors. In the suggested frequency restoration loop, each four-leg power converter measures the frequency level in every sample time and send it to other units. Subsequently, the average value is calculated in each secondary control layer. Finally, the frequency restoration loop can be used as [28]:

$$\delta f_{DG_k} = k_{pf} (f_{microgrid}^* - \bar{f}_{DG_k}) + k_{if} \int (f_{microgrid}^* - \bar{f}_{DG_k}) dt \quad (17)$$

where  $\bar{f}_{DG_k} = \frac{\sum_{i=1}^N f_{DG_i}}{N}$ .  $k_{pf}$  and  $k_{if}$  are the proportional and integral terms of the PI controller,  $f_{microgrid}^*$  is the microgrid frequency reference,  $\bar{f}_{DG_k}$  is the frequency average for all grid-forming power converters, and  $\delta f_{DG_k}$  is the control signal generated by the secondary layer of  $DG_k$  in every sample time. The frequency restoration loop just shifts up the primary response so that frequency reaches to the nominal value, even for the four-leg inverters with different power rates.

Due to variation in the voltage at different points of the islanded microgrid (as opposed to the frequency, which is constant in the network), in the decentralized control method, the reactive power also needs to be measured for each four-leg inverter and shared with other DGs, as with frequency. The reactive power can also be compensated using a similar procedure as the frequency control restoration loop as [28]:

$$\delta Q_{DG_k} = k_{pQ} (\bar{Q}_{DG_k} - Q_{DG_k}) + k_{iQ} \int (\bar{Q}_{DG_k} - Q_{DG_k}) dt \quad (18)$$

where  $\bar{Q}_{DG_k} = \frac{\sum_{i=1}^N Q_{DG_i}}{N}$ .  $k_{pQ}$  and  $k_{iQ}$  are the proportional and integral terms of the PI controller,  $Q_{DG_k}$  is the reactive power of  $DG_k$ ,  $\bar{Q}_{DG_k}$  is average of reactive power for all grid-forming power converters, and  $\delta Q_{DG_k}$  is the control signal generated by the secondary layer in every sample time. The gains of the secondary controller are calculated using the method presented in [28].

## 4. Results and discussion

The proposed hierarchical controller has been implemented in a microgrid, which consists of two three-phase four-leg power converters connected to renewable energy sources (RESs) as shown in Fig. 12. The inductors between each DG and the point of common coupling (PCC) ( $l_{11}$ ,  $l_{12}$ ) model the distribution lines, and a static switch (SS) is used at the PCC to discount microgrid from the rest of distribution network under abnormal conditions. The parameters of the loads, control system for both DGs and microgrid power stage are given in Appendix.

### 4.1. Primary control strategy in grid-connected mode

In this part, the performance of the suggested primary control strategy under unbalanced and nonlinear load conditions in grid-connected mode is investigated. In order to confirm the performance and feasibility of the suggested scheme, a hardware prototype as shown in Fig. 13, has been developed. The test bed consists of the TMS320F28335 Control CARD, a four-leg inverter based on 1.2 kV IGBT and electronic card to sense the currents (LEM LA55-P) and voltages (LEM LV25-P).

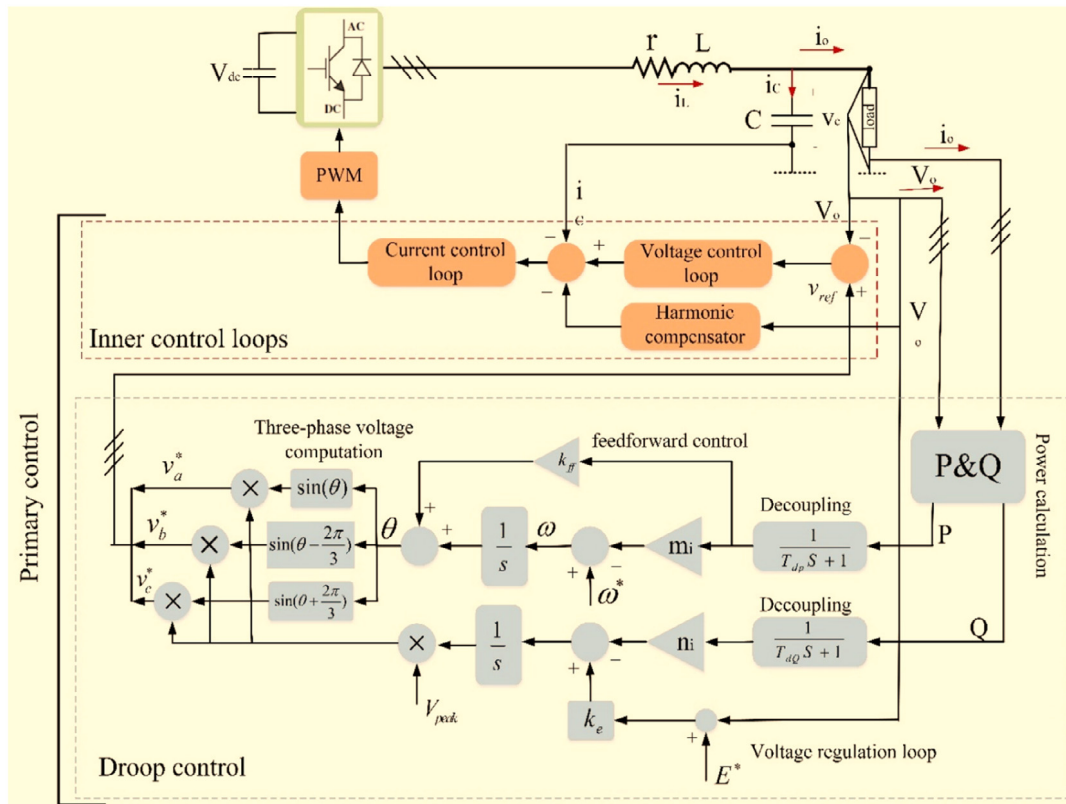


Fig. 10. Scheme of the proposed droop-based power sharing control strategy with inner control loops.

While the SS is closed and DG2 is disconnected from the microgrid, DG1 is supplying a three-phase unbalanced and nonlinear load in the grid-connected mode. For this mode of operation, the power quality at the PCC is very important with the presence of unbalanced and nonlinear loads, and the employed control strategy for the DG1 should be able to compensate unbalanced and harmonic currents at the PCC.

The performance of the suggested primary control strategy under nonlinear load conditions is depicted in Fig. 14. As can be observed, the proposed control strategy can excellently reduce the THD of the PCC. The current THD is reduced from above 21% to lower than 2.4% with the offered control. Fig. 15 also shows the three-phase currents of the grid-connected microgrid at the PCC before and after compensation. As seen, with the proposed control strategy the three-phase currents at the PCC with the load unbalance of 10% become balanced according to the IEEE standards. After compensation the PVUR reached to below 0.5%.

#### 4.2. Primary control strategy under unbalanced load conditions

In this part, DG1 is providing active power for a three-phase resistive load (8 Ω/ph), while DG2 is not connected to the microgrid. Next, at 0.3 s, a single-phase inductive-resistive load (R = 20 Ω and L = 2 mH) is connected between phases ‘a’ and ‘c’. Later, at 0.5 s, the added load between phase ‘c’ and the neutral line is reduced from 8 to 5.7 Ω. Finally, at 0.7 s, the nominal load between phase ‘a’ and the neutral line is disconnected. In this part, for better performance comparison, the desired voltage is 155.56 V line-to-neutral peak at 60 Hz. The performance of the suggested per-phase multi-loop control strategy under unbalanced load conditions is compared with the conventional SCC-based control strategy [22,23,29]. Fig. 16 displays the three-phase output voltages of the DG1 under unbalanced load variations, with the conventional control strategy. As seen, the

load voltages are balanced at first. Next, the load voltages in phases ‘a’ and ‘c’ are reduced by at least 3 line cycles transient as a result of the inclusion of the line-to-line load between phases ‘a’ and ‘c’ at 0.3 s. As seen, a large voltage sag is observed in the output voltages with this control strategy; however, it is repaired with a slow transient response. Next, the load between phase ‘c’ and the neutral line is reduced from 8 to 5.7 Ω at 0.5 s. So, a large voltage sag emerges in the load voltages, and is restored slowly because of the sudden load change. Lastly, the load between phase ‘a’ and the neutral line is separated at 0.7 s. As can be seen, the load disconnection leads to unequal voltage values on three-phases. Nonetheless, the output voltage values are restored with a slow transient response. As seen from figures, at least 3 line cycles transient response exist with this control scheme.

Fig. 17 shows the three-phase output voltages of the DG1 under the condition of sudden load changes with the suggested control strategy. As seen, after the connection of the line-to-line load between phase ‘a’ and ‘c’ at 0.3 s, the output voltages remain balanced without any voltage dip after the sudden load change. Similarly, after the connection of the load between phase ‘c’ and the neutral line at 0.5 s, the output voltages remain balanced under this load changes. Finally, the nominal load between phase ‘a’ and the neutral line is disconnected at 0.7 s. As can be observed, the load voltages can still remain balanced even after this load change. The outcomes prove that the recommended control strategy has the capability to balance the load voltages without any voltage variations under different combinations of unbalanced loads and the position of sudden load changes. As seen, the proposed control system indicates an enhanced dynamic performance in comparison with the conventional control strategy. This is because it is implemented independently in each phase to compensate for the symmetrical components. As seen, the dynamic response of the suggested control scheme is very fast with 1 line cycle transient. The proposed strategy does

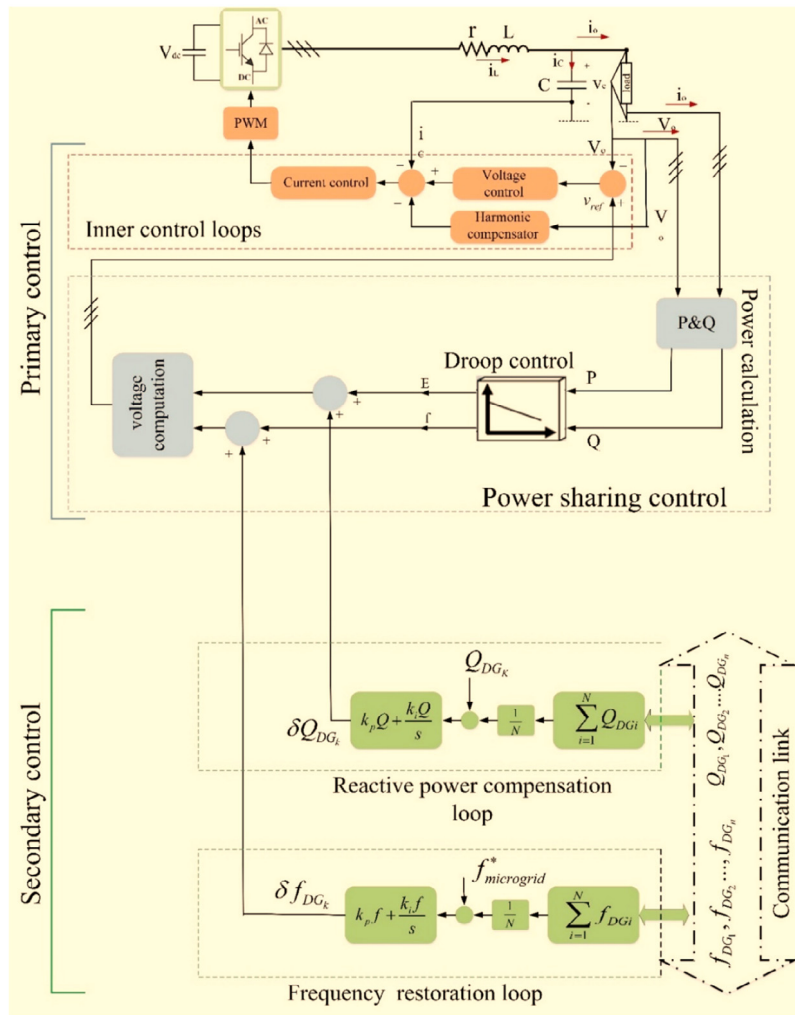


Fig. 11. Scheme of the distributed secondary controller with the primary layer.

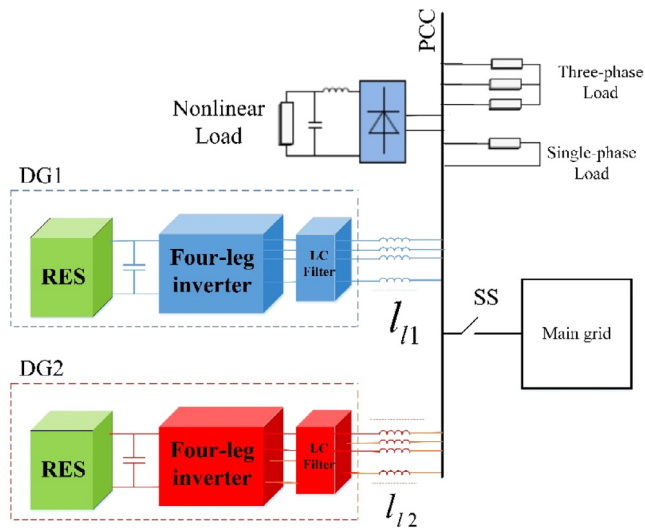


Fig. 12. Microgrid test system for simulations.

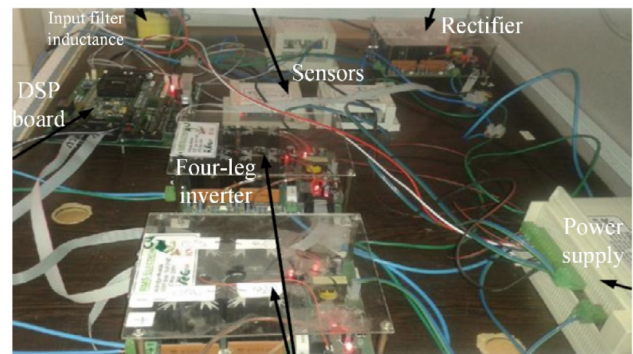


Fig. 13. The laboratory test bed.

realized without using low-pass or all-pass filters, and it is able to attain a fast transient response.

#### 4.3. Power sharing control strategy under unbalanced load conditions

In this test, while the islanded microgrid is initially operating under no-load conditions, the three-phase unbalanced inductive-resistive load#3, with the active power of 5.4 kW and reactive

not require computations for the symmetrical components of currents and voltages for unbalanced voltage compensation. It is

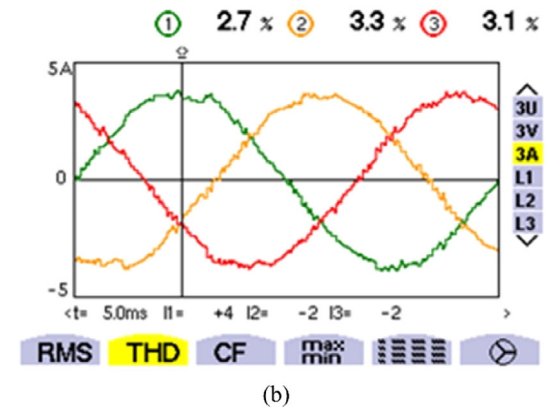
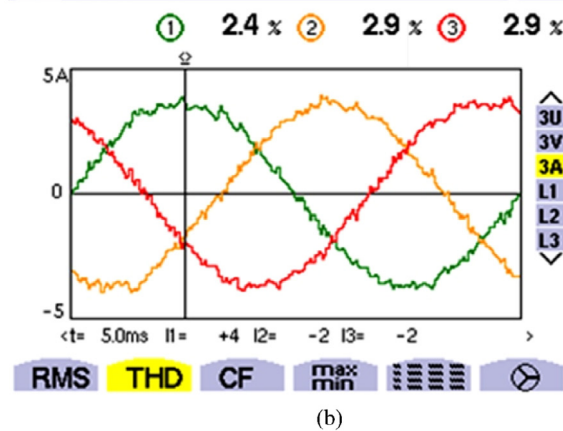
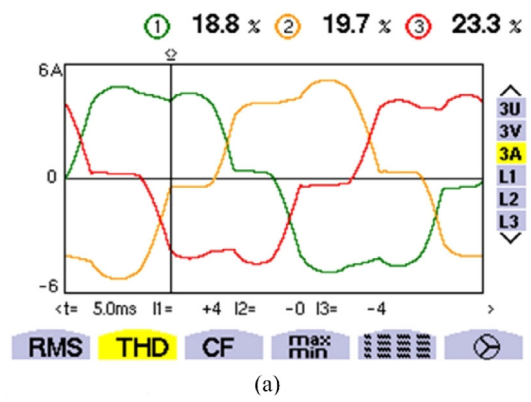
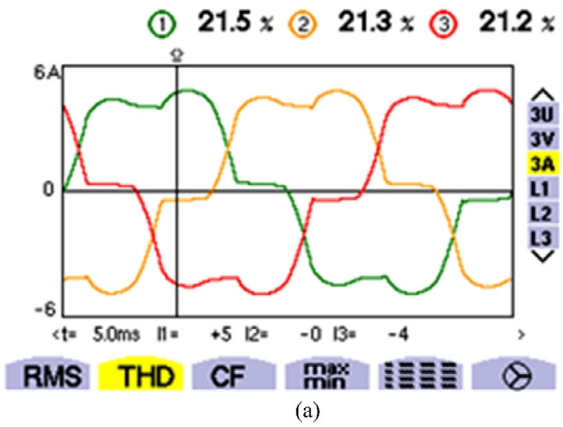


**Fig. 14.** Source current waveform in grid-connected microgrid under nonlinear load condition, (a) without harmonic compensator, (b) with the proposed harmonic compensator.

**Fig. 15.** Source current waveform at the PCC in the grid-connected microgrid under unbalanced and nonlinear load condition, (a) without primary control compensator, (b) with the proposed primary control compensator.

power of 1.2 kVar, is suddenly connected to the PCC at 1 s. Later, at 3 s, the single-phase inductive–resistive load#4, with the active power of 1.8 kW and reactive power of 0.4 kVar, is connected between phase ‘c’ and the neutral line at the PCC. The desired voltage is 170 V line-to-neutral peak at 50 Hz and both DGs are connected to the microgrid. The parameters of loads, and the control system for both DGs and microgrid power stage are given in Appendix.

The output real and reactive powers of the DGs during the load switching are depicted in Fig. 18. It is observed that the active power is accurately shared between the DGs under unbalanced load conditions, because the frequency is a global variable in the whole microgrid. As seen in this figure, the active powers in both DGs are sharply raised subsequent to the connection of the three-phase unbalanced load#3 at 1 s. It can be observed that a double-frequency ripple appears in the instantaneous active power components, after the addition of the three-phase unbalanced load. The active power is increased again sharply at 3s because of the connection of the single-phase load#4. The double-frequency ripple is also raised at 3 s, owing to the inclusion of the single-phase load.

The reactive power is also shared between the DGs with the least possible value for reactive power sharing error. This reactive power-sharing error is because of the fact that the voltage is not common in the whole microgrid. It is also observed that the reactive powers in both DGs are suddenly increased, when the three-phase unbalanced load and the single-phase load are suddenly connected to the PCC at 1 s and 3 s, respectively. A

double-frequency ripple is seen in the instantaneous reactive power components at 1 s caused by the inclusion of the unbalanced load. This ripple is increased again at 3 s because of the inclusion of the single-phase load. As seen, the proposed power sharing unit is capable of accurately sharing the active and reactive powers between the DGs under unbalanced load conditions. However, a reactive power-sharing error exists between the DGs, which can be compensated using the secondary controller.

The output waveforms of DG1, equipped with the proposed primary control strategy, are shown in Fig. 19. The transient load voltages and currents are shown as zoomed figures. As can be observed from this figure, the three-phase output currents are sharply increased at 1 s because of connection of three-phase unbalanced loads. Afterwards, the output currents are rapidly changed as a consequence of the connection of the single-phase load between phase ‘c’ and the neutral at 3 s. It is surprising to see that the output voltages of the DG1 remain balanced under all unbalanced load changes. Overall, the results mentioned in this part of the study have indicated that the proposed primary controller, which consists of the per-phase multi-loop control strategy, and the power-sharing unit, has the ability to share power accurately between the DGs.

#### 4.4. Primary control approach under nonlinear load conditions

In this part, a single-phase nonlinear load that contains of a diode rectifier bridge that feeds a 500  $\mu$ F capacitor in parallel with a 30  $\Omega$  resistor, is connected between phase ‘a’ and the neutral line at the PCC. Multi-resonant harmonic voltage compensator with the same specifications are activated for both

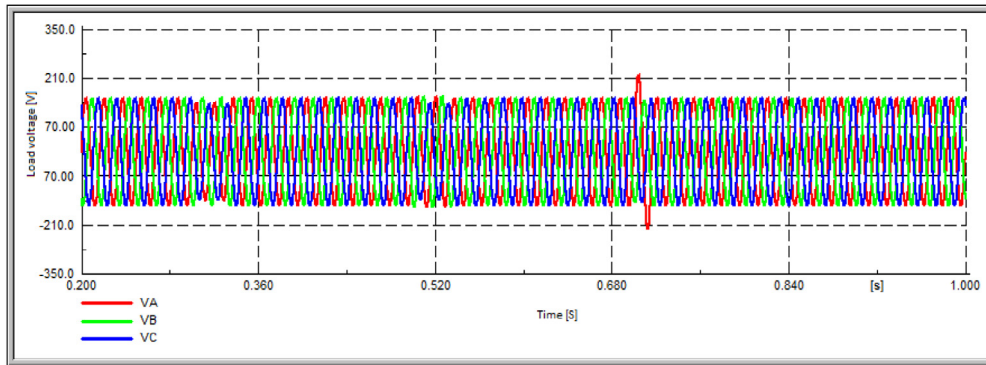


Fig. 16. Output voltages with the conventional control strategy.

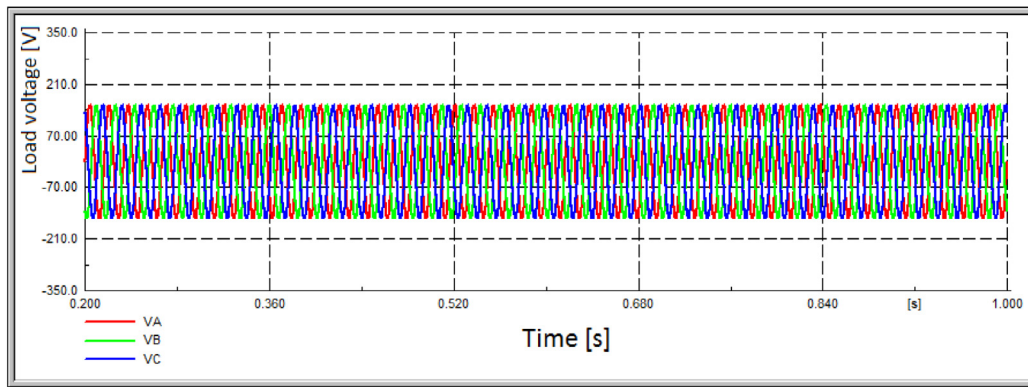


Fig. 17. Three-phase output voltages with the proposed control strategy.

DGs. Moreover, they have the same power rating. The controller parameters for both DGs are given in Appendix. Fig. 20 shows the output voltages of phase ‘a’ in the DGs and their harmonic spectra, before using the harmonic compensator. As observed, negative and zero sequence harmonics, containing the 3rd, 5th, 7th, 9th, 11th and 13th harmonics, can result in power quality challenge in the islanded microgrid. The output voltage quality for both DGs can be enhanced using the suggested scheme.

Fig. 21 also depicts the output voltage of phase ‘a’ in the DGs and their harmonic spectra, with the proposed harmonic controller. As seen, using the proposed compensator, the harmonics for voltages in the 3rd, 5th, 7th, 9th, 11th and 13th harmonics are perceptibly suppressed. As seen, the output voltage of DG1 remains sinusoidal after compensation, and the THD is reduced from 5.9% to 2.68%. Moreover, by using the suggested harmonic controller, the THD of DG2 is reduced from 5.1% to 2.55%.

#### 4.5. Secondary control strategy

In this part, the secondary control strategy has been simulated using the DigSILENT PowerFactory software. The three-phase four-leg power converters are equipped with the proposed hierarchical control strategy. In the following, the performance of the reactive power compensation and the frequency restoration loops at the secondary level are investigated. In this simulation, while the microgrid is initially operating under no-load circumstances, the three-phase inductive–resistive load#1, with the active power of 5.4 kW and reactive power of 1.2 kVar, is suddenly connected to the PCC at 0.5 s. The primary controllers share the active and reactive powers between four-leg power converters subsequent to the connection of the load. As the primary level cannot achieve zero reactive power sharing error on its own in the islanded mode, the reactive power compensator

at the secondary layer is employed to compensate the reactive power sharing error. Therefore, the reactive power compensation controller in the secondary layer is activated at 1.5 s.

The performance of the reactive power compensation controller, when applied to the microgrid, is depicted in Fig. 22. As seen, the real and reactive powers in both DGs are sharply increased at 0.5s, after the addition of the load to the PCC. This load connection leads to a decrease in the frequency of the DGs due to the operation of the active power/frequency control loop at the primary layer. Similarly, the output voltages of the DGs are also reduced because of the operation of the reactive power/voltage control loop at the primary layer.

As seen, the active power can be shared equally between two DGs using the proposed primary controller with the ratio of 1:1. It can be seen that both DGs have the same frequency prior and subsequent to the connection of the load. However, it is observed that the reactive power cannot be precisely shared between these DG units using the primary controller. This is due to the fact that the voltage is not common in the whole microgrid. As seen, an error exists between the values of the reactive powers in DG1 and DG2, before the activation of the reactive power compensation loop at the secondary controller.

Moreover, the reactive power compensator at the secondary controller is activated at 1.5 s. As seen, the reactive power can be very accurately shared between two DG units with zero sharing error after the reactive power compensator is activated. It is observed that the accuracy of the reactive power-sharing is significantly improved with a ratio of 1:1, using the primary and secondary controllers. Table 1 compares the values of the reactive powers in the DGs, before and after the activation of the secondary controller. As can be seen in this table, there is 0.023 kVar of reactive power-sharing error between the DGs using

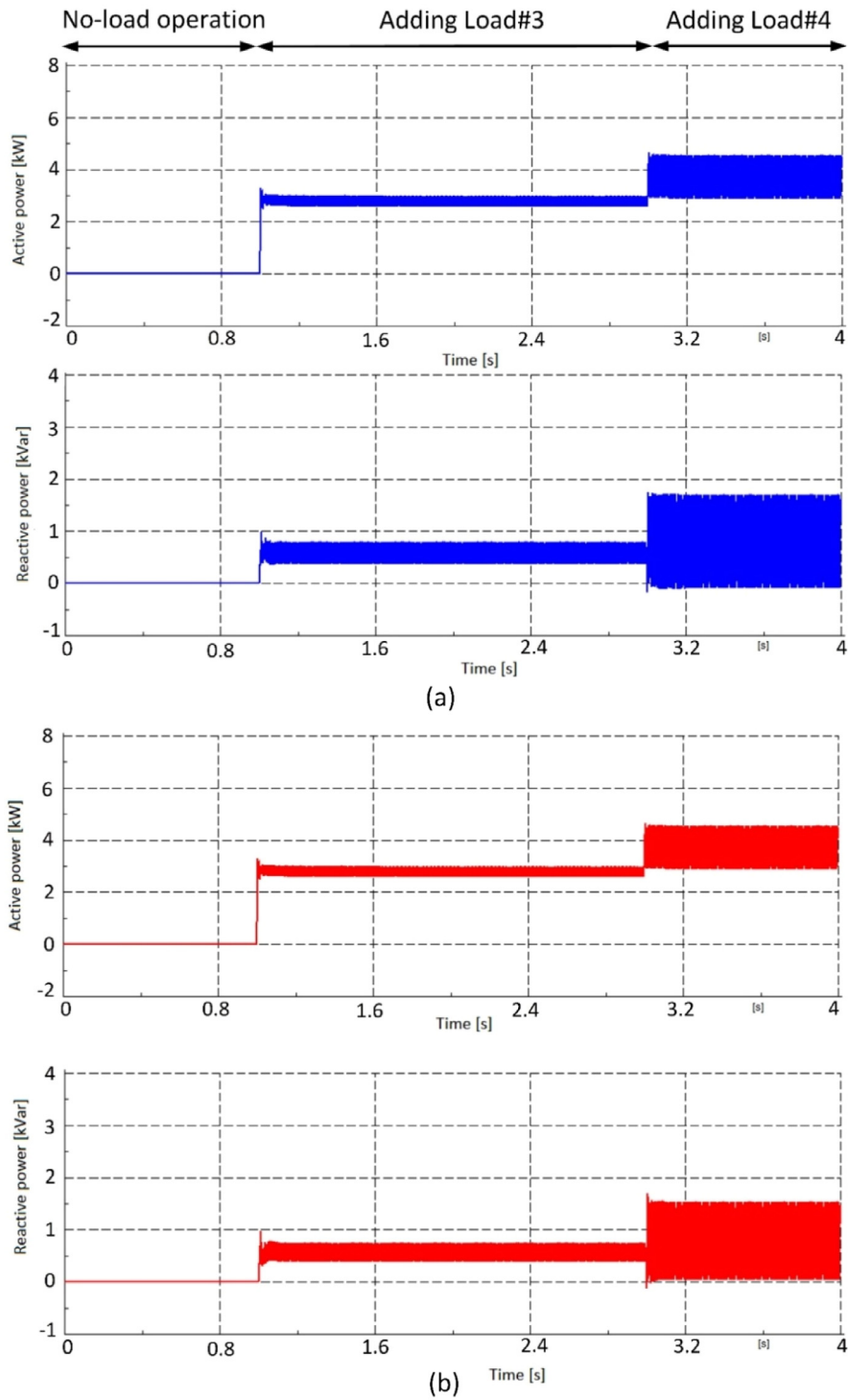


**Fig. 18.** Performance of the proposed power sharing control strategy under unbalanced load conditions. (a) Active and reactive power sharing in DG1. (b) Active and reactive power sharing in DG2.

**Table 1**  
Comparison of reactive power sharing in DGs with and without using the reactive power compensation loop in the secondary controller.

Power-sharing control method	Reactive power of DG1 [kVar]	Reactive power of DG2 [kVar]
With the primary controller	0.609	0.586
With the primary and secondary controller	0.599	0.599

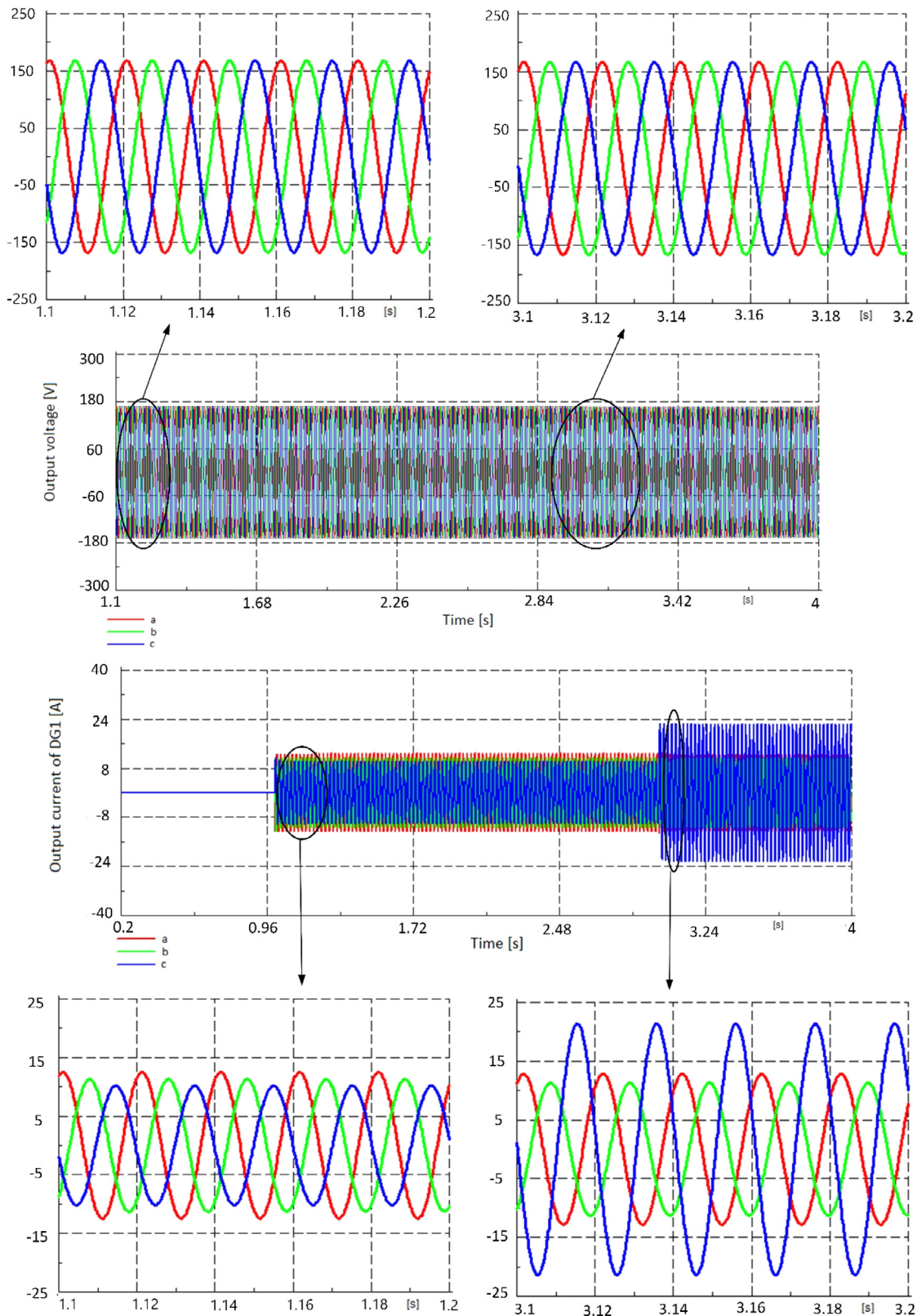
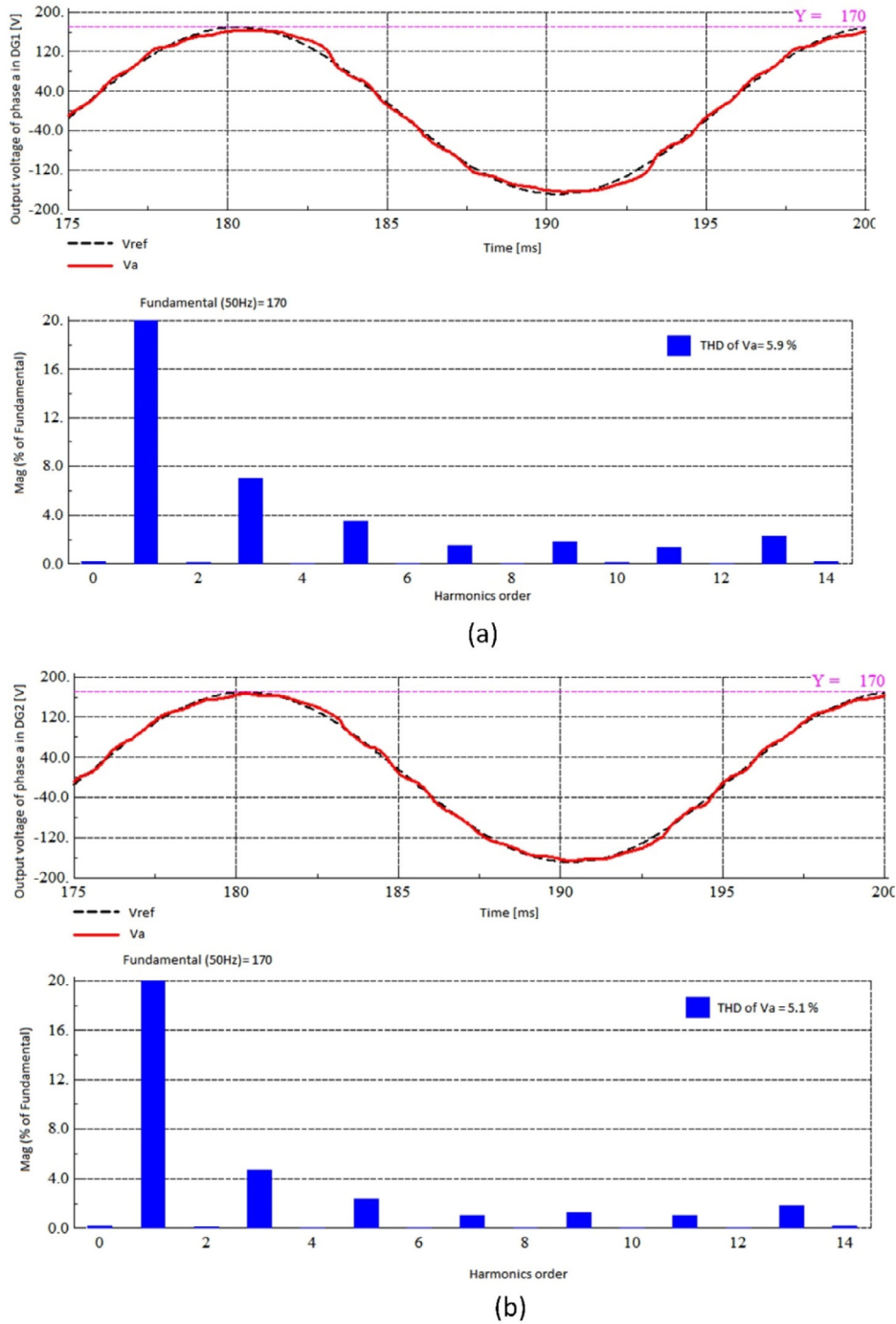


Fig. 19. Output voltages and currents of DG1 under unbalanced load conditions.

the primary controller, and before the activation of the reactive power compensation loop in the secondary layer. In contrast, the reactive powers have same values in both DGs, after the activation of the reactive power compensation loop. The results

of this investigation show that the precise reactive power sharing can be achieved using the primary and the secondary controllers.

To study the performance of the frequency restoration loop, the three-phase inductive–resistive load#5, with the active power



**Fig. 20.** Output voltage of phase 'a', without using the harmonic compensation loop. (a) Output voltage of phase 'a' in DG1 and the associated voltage harmonic spectrum. (b) Output voltage of phase 'a' in DG2 and the associated voltage harmonic spectrum.

of 10.8 kW and reactive power of 2.4 kVar, is suddenly connected to the PCC at 2 s. The frequency restoration loop at the secondary controller is then activated at 4.5 s to restore the frequency deviations produced by the primary controller. It should be noted here that the reactive power compensation loop at the secondary layer is simultaneously activated to compensate the reactive power-sharing error. Therefore, the active and reactive powers can be accurately shared between the DGs using the primary and secondary controllers.

The performance of the distributed frequency restoration loop that is applied to the microgrid is depicted in Fig. 23. As seen

in this figure, the frequencies of both DGs are sharply reduced after the inclusion of the load at 2 s. This sudden reduction is because of the action of the active power/frequency controller. As seen, the frequency restoration loop at the secondary controller is activated at 4.5 s for both DG units to restore the frequency deviation caused by the primary controller. The frequency values are observed to be slowly and accurately regulated after activating the frequency restoration controller at the secondary controller. The simulation results show that this loop at the secondary layer can successfully restore the frequency deviations caused by the primary controller inside the microgrid.

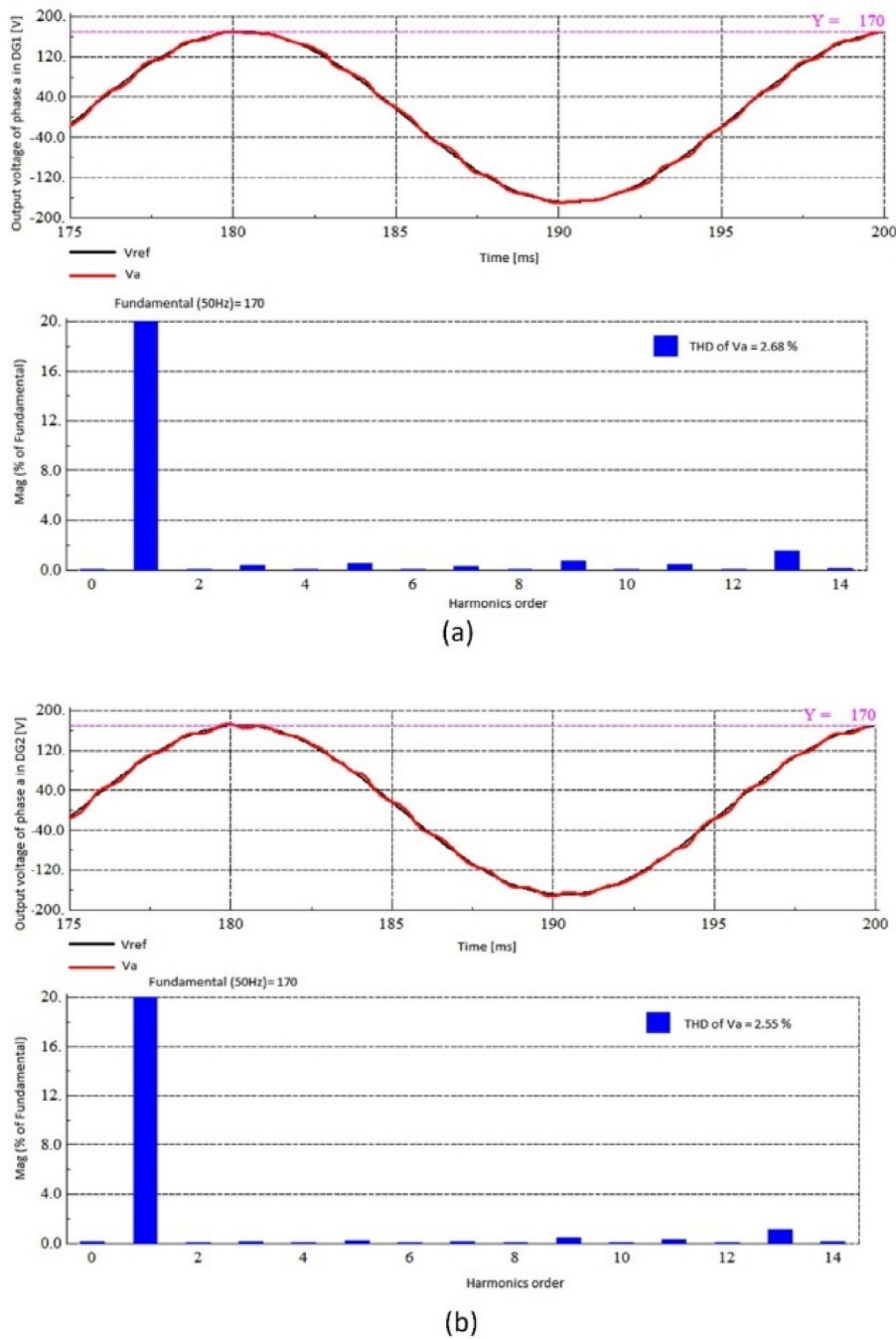


**Fig. 21.** Output voltage of phase ‘a’ with the proposed harmonic compensation loop. (a) Output voltage of phase ‘a’ in DG1 and the associated voltage harmonic spectrum. (b) Output voltage of phase ‘a’ in DG2 and the associated voltage harmonic spectrum.

**5. Conclusion**

This research has proposed an enhanced primary and secondary control schemes for a three-phase 4-wire islanded microgrid. The suggested primary and secondary controllers can perfectly support the operation of the three-phase 4-wire islanded microgrids under unbalanced and nonlinear load conditions. The hierarchical controller was able to enhance the operation stability of three-phase 4-wire islanded microgrids by achieving accurate active and reactive power-sharing with zero reactive power-sharing error. The proposed hierarchical control strategy

has offered several advantages, and the following observations can be highlighted:

- The superiority of the proposed control strategy over the conventional SCC-based control scheme was confirmed by the 2 line cycles decrease in the transient response
- The compensation of both negative and zero sequence harmonics, simple control structure and insensitivity to frequency variations have given this control scheme an edge over the conventional control strategies. The voltage THD of the grid-forming power converters were reduced from

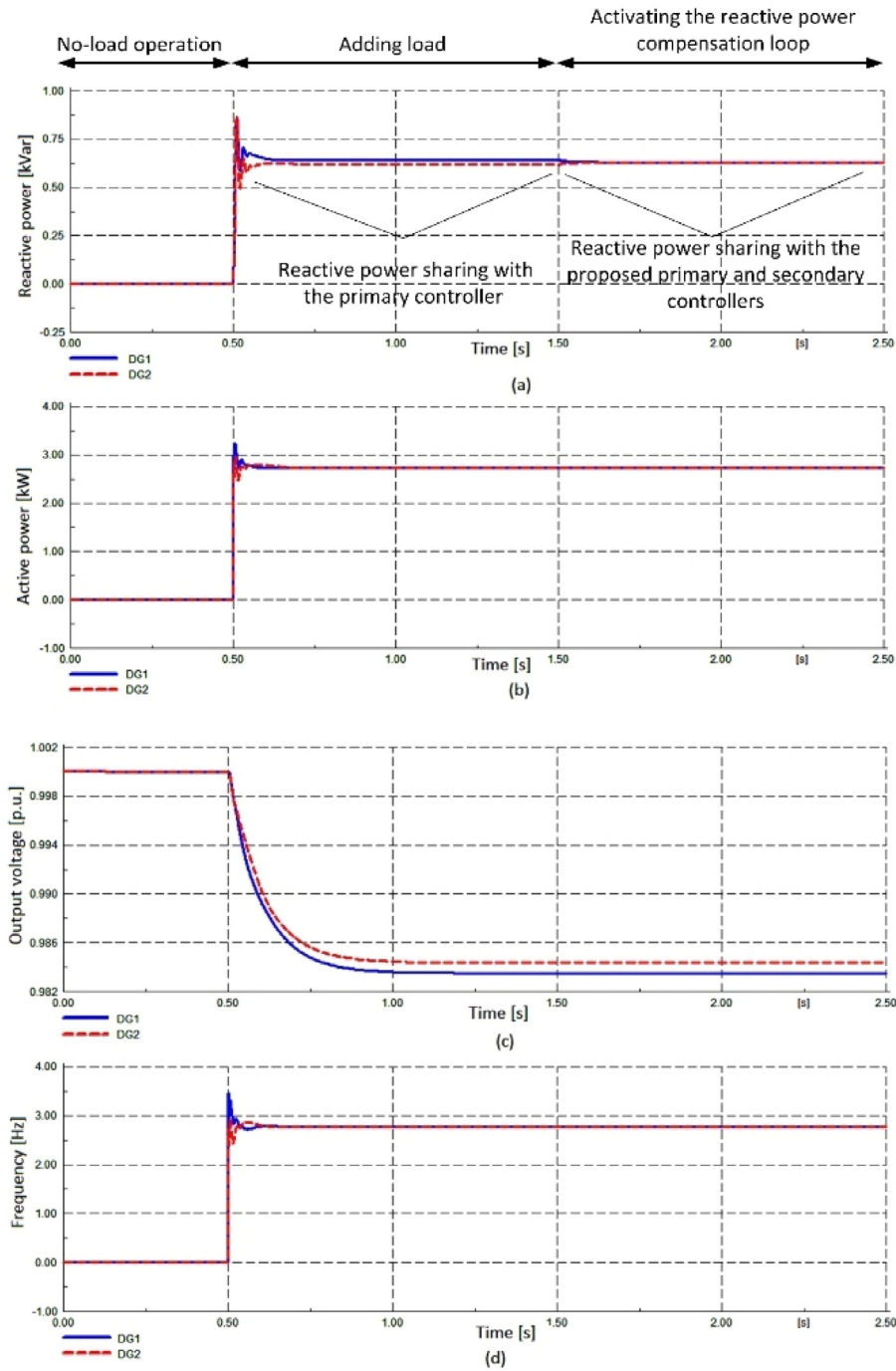


Fig. 22. Performance of the reactive power compensation loop. (a) Reactive power compensation. (b) Active power. (c) Voltage amplitude. (d) Frequency.

above 5.1% to lower than 2.7% with the suggested controller under nonlinear load situations.

- Zero reactive power-sharing error has given this control strategy an edge over the conventional droop control scheme in three-phase 4-wire islanded microgrids.

**Acknowledgements**

The authors wish to thank the Ministry of Education (MOE), Malaysia and Universiti Teknologi Malaysia under the Post-Doctoral Fellowship Scheme grant numbers, 4F828, 04E54, and 18H10 for the financial support.

**Conflict of interest**

The authors declare that they have no known competing financial interests or personal relationships that could have appeared to influence the work reported in this paper.

**Appendix**

The parameters of the four-leg inverter, loads, control system for microgrid power stage are: DC bus voltage: 300 V, filter capacitance: 300 μF, filter inductance: 0.1 mH, resistors of the filter: 10 mΩ,  $l_{f1}$ : 0.5 mH,  $l_{f2}$ : 0.75 mH, load#1: 5.4 kW + 1.2 kVar,

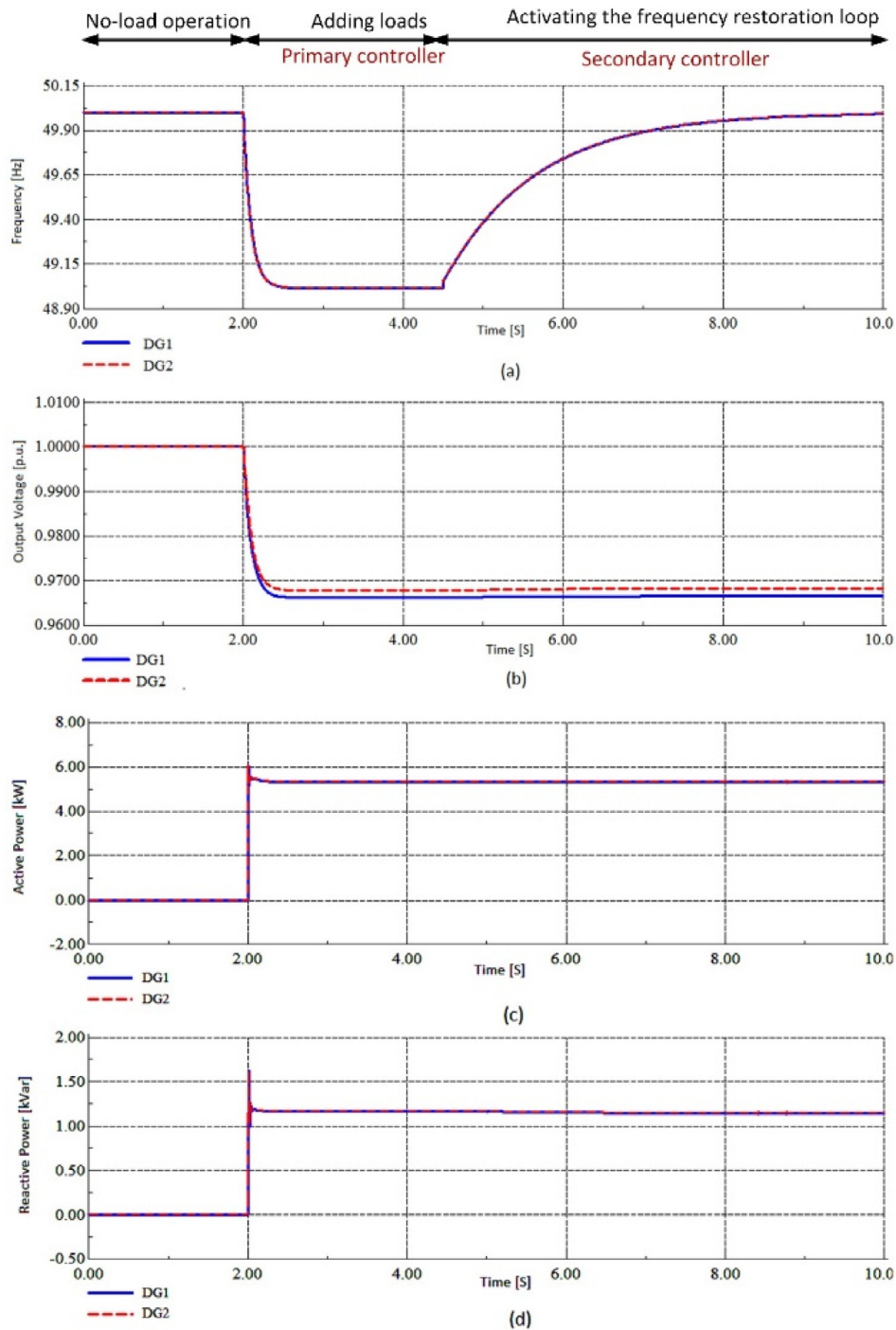


Fig. 23. Performance of the frequency restoration loop. (a) Frequency restoration. (b) Voltage amplitude. (c) Active power. (d) Reactive power.

load#2: 5.4 kW + 1.2 kVar, load#3: 5.4 kW + 1.2 kVar, load#4: 1.8 kW + 0.4 kVar, load#5: 10.8 kW + 2.4 kVar, Nonlinear load:  $C = 500 \mu F$ ,  $R = 30 \Omega$ , current controller parameter:  $K = 1$ , PI voltage controller parameters: ( $K_p = 0.15, K_I = 42$ ),  $m_i$ : 0.00116 rd/Ws,  $n_i$ : 0.000027 p.u./Var,  $k_{ff}$ :  $-0.0056$  rad/W,  $k_e$ : 4,  $k_n$ : ( $k_3 = 75, k_5 = 50, k_7 = 25, k_9 = 20, k_{11} = 15, k_{13} = 10$ ),  $k_{pf}$ : 0.25,  $k_{ff}$ : 5,  $k_{pQ}$ : 0.1,  $k_{iQ}$ : 10.

References

[1] Tabbache B, et al. An improved fault-tolerant control scheme for PWM inverter-fed induction motor-based EVs. ISA Trans 2013;52(6):862–9.

[2] Miveh MR, et al. Control techniques for three-phase four-leg voltage source inverters in autonomous microgrids: A review. Renew Sustain Energy Rev 2016;54:1592–610.

[3] Miveh MR, et al. Power quality improvement in autonomous microgrids using multi-functional voltage source inverters: a comprehensive review. J Power Electron 2015;15(4):1054–65.

[4] Hosseinzadeh M, Salmasi FR. Fault-tolerant supervisory controller for a hybrid AC/DC micro-grid. IEEE Trans Smart Grid 2016.

[5] Hosseinzadeh M, Salmasi FR. Robust optimal power management system for a hybrid AC/DC micro-grid. IEEE Trans Sustain Energy 2015;6(3):675–87.

[6] Kohn W, Zabinsky ZB, Nerode A. A micro-grid distributed intelligent control and management system. IEEE Trans Smart Grid 2015;6(6):2964–74.

- [7] Eghtedarpour N, Farjah E. Power control and management in a hybrid AC/DC microgrid. *IEEE Trans Smart Grid* 2014;5(3):1494–505.
- [8] Hosseinzadeh M, Salmasi FR. Power management of an isolated hybrid AC/DC micro-grid with fuzzy control of battery banks. *IET Renew Power Gener* 2015;9(5):484–93.
- [9] Chebabhi A, et al. Comparative study of reference currents and DC bus voltage control for Three-Phase Four-Wire Four-Leg SAPF to compensate harmonics and reactive power with 3D SVM. *ISA Trans* 2015;57:360–72.
- [10] Chebabhi A, et al. A new balancing three level three dimensional space vector modulation strategy for three level neutral point clamped four leg inverter based shunt active power filter controlling by nonlinear back stepping controllers. *ISA Trans* 2016;63:328–42.
- [11] IEEE Recommended Practice for Monitoring Electric Power Quality, IEEE Std. 1159, 2009.
- [12] IEEE Recommended Practice for Electric Power Distribution for Industrial Plants, ANSI/IEEE Std. 141, 1993.
- [13] IEEE Recommended Practices and Requirements for Harmonic Control in Electrical Power Systems, IEEE Standard 519-1992.
- [14] Naderipour A, et al. A harmonic compensation strategy in a grid-connected photovoltaic system using zero-sequence control. *Energies* 2018;11(10):2629.
- [15] Ho CN-M, Cheung VS, Chung HS-H. Constant-frequency hysteresis current control of grid-connected VSI without bandwidth control. *IEEE Trans Power Electron* 2009;24(11):2484–95.
- [16] Liu T, et al. A novel repetitive control scheme for three-phase grid-connected inverter with LCL filter. In: *Power electronics and motion control conference, IPERC, 2012 7th international*. IEEE; 2012.
- [17] Yaramasu V, et al. High performance operation for a four-leg NPC inverter with two-sample-ahead predictive control strategy. *Electr Power Syst Res* 2015;123:31–9.
- [18] Umamaheswari MG, Uma G, Vijayalakshmi KM. Analysis and design of reduced-order sliding-mode controller for three-phase power factor correction using Cuk rectifiers. *IET Power Electron* 2013;6(5):935–45.
- [19] Matas J, et al. Feedback linearization of a single-phase active power filter via sliding mode control. *IEEE Trans Power Electron* 2008;23(1):116–25.
- [20] Yang L-Y, et al. Sliding mode control of three-phase four-leg inverters via state feedback. *J Power Electron* 2014;14(5):1028–37.
- [21] Lei H, et al. Research on paralleled three-phase four-leg voltage source inverters based on dual-loop control in  $\alpha\beta o$  coordinate. In: *Power electronics and ECCE Asia, ICPE & ECCE, 2011 IEEE 8th international conference on*. IEEE; 2011.
- [22] Vechiu I, et al. Control of four leg inverter for hybrid power system applications with unbalanced load. *Energy Convers Manage* 2007;48(7):2119–28.
- [23] Vechiu I, Curea O, Camblong H. Transient operation of a four-leg inverter for autonomous applications with unbalanced load. *IEEE Trans Power Electron* 2010;25(2):399–407.
- [24] Cárdenas R, et al. Control of a matrix converter for the operation of autonomous systems. *Renew Energy* 2012;43:343–53.
- [25] Rodríguez P, et al. Multiresonant frequency-locked loop for grid synchronization of power converters under distorted grid conditions. *IEEE Trans Ind Electron* 2011;58(1):127–38.
- [26] Golestan S, et al. A DQ synchronous frame controller for single-phase inverters. In: *Power electronics, drive systems and technologies conference, PEDSTC, 2011*. IEEE; 2011.
- [27] Zhong QC, Hornik T. Harmonic droop controller to improve voltage quality. In: *Control of power inverters in renewable energy and smart grid integration*. 2013, p. 347–58.
- [28] Shafiee Q, Guerrero JM, Vasquez JC. Distributed secondary control for islanded microgrids—A novel approach. *IEEE Trans Power Electron* 2014;29(2):1018–31.
- [29] Vechiu I, Etxeberria A, Tabart Q. Power quality improvement using an advanced control of a four-leg multilevel converter. In: *Control and modeling for power electronics, COMPEL, 2015 IEEE 16th workshop on*. IEEE; 2015.